

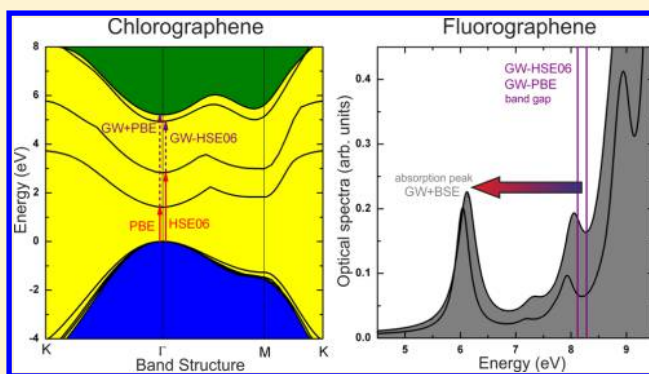
# Band Gaps and Optical Spectra of Chlorographene, Fluorographene and Graphane from $G_0W_0$ , $GW_0$ and GW Calculations on Top of PBE and HSE06 Orbitals

František Karlický\* and Michal Otyepka\*

Regional Centre of Advanced Technologies and Materials, Department of Physical Chemistry, Faculty of Science, Palacký University, Tř. 17. listopadu 12, Olomouc 771 46, Czech Republic

## S Supporting Information

**ABSTRACT:** The band structures of three graphene derivatives (chlorographene, fluorographene, and graphane) were analyzed at three levels of many-body GW theory ( $G_0W_0$ ,  $GW_0$ , and GW) constructed over GGA (PBE) and screened hybrid HSE06 orbitals. DFT band gap values obtained with the HSE06 functional were notably larger than those from PBE calculations but were significantly lower than band gaps from all GW calculations. On the other hand, all GW-type calculations gave similar band gaps despite some differences in band structures. The band gap (4.9 eV at the highest GW-HSE06 level) was predicted to be smaller than that of fluorographene (8.3 eV) or graphane (6.2 eV). However, chlorographene can be considered a wide-band gap insulator analogous to fluorographene and graphane. Using the Bethe–Salpeter equation, optical absorptions of graphene derivatives were found to be at significantly lower energies due to large binding energies of excitons (1.3, 1.9, and 1.5 eV for chlorographene, fluorographene, and graphane, respectively). Point defects lowered band gaps and absorption energies. Taking into account the low concentration of defects in this type of material, their effect on the discussed electronic properties was rather small.



## INTRODUCTION

Covalently modified graphene derivatives prepared by attachment of hydrogen and halogens have attracted considerable interest over the past few years because of their potential applications (e.g., in electronic devices).<sup>1,2</sup> The attachment of atoms to  $sp^2$  carbons changes its hybrid state to  $sp^3$ , which significantly alters the electronic properties and local structure but preserves the 2D hexagonal symmetry. Such structural changes induce opening of the zero band gap of graphene at the K point and lead to loss of the  $\pi$ -conjugated electron cloud present above and below graphene plane. Recently, fully hydrogenated graphene (graphane, CH)<sup>3,4</sup> and fully fluorinated graphene (fluorographene, also known as graphene fluoride, CF) have been successfully prepared.<sup>5–8</sup> In contrast, the fully chlorinated counterpart has not yet been prepared and partially chlorinated graphene derivatives have only very recently been reported.<sup>9,10</sup> Generally, wide band gap materials, such as CF, CH, or BN, may be useful as 2D insulators for creating semiconductor/insulator interfaces suitable for the development of nanosized field-effect transistors (FETs).<sup>11</sup> Recently proposed graphene-based ultracapacitors<sup>12</sup> also highlight the importance of 2D insulator research.

Despite numerous theoretical and experimental studies, much is still unknown about the electronic structure of these types of materials. Therefore, we investigated the electronic structure and band gaps of 2D halogenated graphene

compounds. Standard generalized gradient approximation (GGA) to density functional theory (DFT) gives a band gap value for CF only half that calculated using a high-level many-body GW<sup>13</sup> approximation (GWA; Table 1),<sup>14–18</sup> which includes electron–electron (e–e) interactions beyond DFT. The CH band gap predicted by GWA is also much larger than values obtained by using local density approximation (LDA) or GGA of Perdew–Burke–Ernzerhof (PBE).<sup>14,15,17,19–21</sup> More-

**Table 1. Summary of Calculated and Experimental Band Gaps,  $E_g$  (in eV), for Graphane (CH), and Fluorographene (CF) based on a Literature Survey<sup>a</sup>**

method	CH	CF
DFT(PBE)	3.5	3.1
DFT(HSE06)	4.5	5.1
$GW_0$ , $G_0W_0$	5.4–6.1	7.3–7.5
BSE- $G_0W_0$ (optical spectra)	3.8	5.4, 3.8
exp. (optical spectra)		>3.8, >3.0 <sup>b</sup>
exp. (density of states)		>3.8 <sup>c</sup>
exp. (transport measurement)		~3 <sup>d</sup>

<sup>a</sup>For details, see ref 22. <sup>b</sup>Optical band gaps, refs 7 and 27.

<sup>c</sup>Fundamental band gap, ref 27. <sup>d</sup>For  $C_{21}F$ , ref 28.

Received: March 21, 2013

Published: July 10, 2013



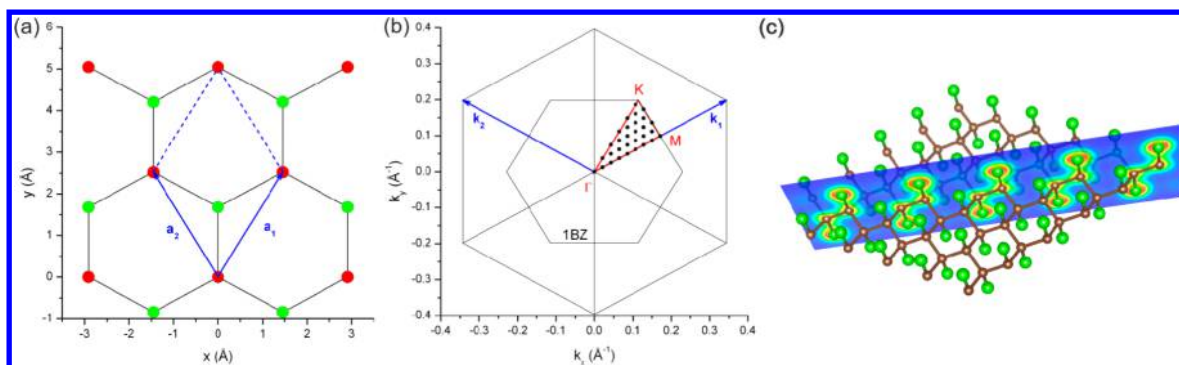


**Figure 1.** (a) Geometrical structure (top view) of chlorographene (CCl) including the translation vectors ( $a_1$  and  $a_2$ ) and elementary cell (blue). The different colors represent chlorine above and below the graphene plane. (b) First Brillouin zone (1BZ) of CCl, basis vectors ( $k_1$  and  $k_2$ ), and high-symmetry points  $\Gamma$ ,  $M$ , and  $K$  in reciprocal space. Black points correspond to original  $16 \times 16$   $k$ -point grid sampling of the 1BZ reduced by VASP to 30 points using  $D_{3d}$  symmetry. (c) Tilted view of the  $5 \times 5$  supercell of CCl and a  $(1\bar{1}0)$  plane (blue) used to construct the electron density cuts shown in Figure 2.

over, GWA predicts that the band gap of CF is greater than that of CH, whereas GGA functionals give the opposite trend (Table 1).<sup>22</sup> Using the Bethe–Salpeter equation (BSE)<sup>23,24</sup> on top of GWA, which accounts for electron–electron and electron–hole (e–h) correlations, the first exciton peaks in the CF and CH absorption spectrum have been predicted to lie between the PBE and GWA band gap values<sup>16,18,20</sup> (Table 1), but without inclusion of e–h interactions (RPA over GW), are close to GWA band gap values. BSE predicts the same trend of band gaps as GWA:  $E_g(\text{CF}) > E_g(\text{CH})$ . In a previous paper,<sup>22</sup> we showed that it is possible to obtain the same order of band gaps with DFT as from GW and BSE if a screened hybrid functional, such as those developed by Heyd, Scuseria, and Ernzerhof (HSE03,<sup>25</sup> HSE06<sup>26</sup>), is used (Table 1).

Despite considerable research efforts, several questions remain unanswered: (i) How do the results depend on the level of GWA calculations ( $G_0W_0$ ,  $GW_0$ , and GW)? (ii) Are the predicted values (GGA DFT band gaps are only half of band gaps calculated using GWA; Table 1) different when HSE orbitals are used in the GWA calculation? (iii) Is the discrepancy between GGA DFT and GWA values observed for different adsorbed halogens? (iv) Are the band gaps of the studied systems significantly lowered in the presence of point defects? In this work, we addressed all the above-mentioned questions. We calculated the band gaps for CH, CF and CCl by GWA over HSE06 orbitals and extended the previously published GWA-PBE results for other graphene derivatives by considering the fully chlorinated graphene (chlorographene, CCl). We systematically investigated the effects of using  $G_0W_0$ ,  $GW_0$ , and GW levels of many-body GWA in modeling the aforementioned materials. Finally, we evaluated absorption spectra from BSE on top of various levels of GWA and discussed the role of excitons and point defects for comparison of theoretical and experimental optical gaps.

## METHODS

GGA functionals systematically underestimate Kohn–Sham band gaps (compared to experimentally determined values), whereas the Hartree–Fock (HF) method systematically overestimates them.<sup>29</sup> Therefore hybrid functionals, which describe exchange using a mixture of the exact nonlocal HF exchange ( $E_x^{\text{HF}}$ ) and GGA exchange functional ( $E_x^{\text{GGA}}$ ), have been developed. Hybrid functionals often give reasonably accurate predictions of band gaps, lead to more accurate total

energies and geometries. However, such functionals are computationally demanding because of the slow decay of the HF exchange, and therefore are intractable for extended systems.<sup>30</sup> Thus, short-range functionals, such as the screened hybrid functional HSE06,<sup>26</sup> seem to be an effective alternative to standard hybrid functionals. In HSE06, the spatial decay of the HF exchange interaction is accelerated by substitution of the full  $1/r$  Coulomb potential with a screened one, the exchange energy term is split into short-range (SR) and long-range (LR) components and the HF long-range component is neglected but compensated by the PBE long-range contribution. The exchange–correlation energy is therefore calculated as

$$E_{\text{xc}}^{\text{HSE06}} = \frac{1}{4}E_x^{\text{HF,SR}}(\omega) + \frac{3}{4}E_x^{\text{PBE,SR}}(\omega) + E_x^{\text{PBE,LR}}(\omega) + E_c^{\text{PBE}} \quad (1)$$

where  $E_c^{\text{PBE}}$  is the PBE correlation energy and  $\omega = 0.11 \text{ bohr}^{-1}$  is the screening parameter.<sup>26</sup> The HSE functional has been shown to accurately predict the electronic properties of low-dimensional carbon materials and optical transitions in both metallic and semiconducting single-wall carbon nanotubes.<sup>31</sup> It has also been studied and compared to GGA for its use as a starting point in the calculation of quasiparticle (QP) excitation energies of 3D materials. Single-shot  $G_0W_0$  calculations following calculations using the HSE03 functional have been shown to give values very close to experiment.<sup>32</sup>

In the present work, the Vienna ab initio simulation package (VASP)<sup>33</sup> implementing the projector augmented waves (PAW) method<sup>34</sup> was used to perform single-point energy GWA calculations on geometries from PBE/HSE06. In all cases, the species were initially assumed to adopt a chairlike conformation (Figure 1a and c for CCl) because it has been shown to be the most stable conformation of both CH and CF.<sup>15,19</sup> The optimized unit cell was obtained by minimizing the total energy as a function of the lattice parameter. For each value of the lattice constant, atomic positions (i.e., internal degrees of freedom) were relaxed until the change in energy was less than  $1 \times 10^{-5}$  eV per cell (break condition for the electronic step was an energy difference of  $1 \times 10^{-6}$  eV). Band structures were typically obtained by subsequent nonself-consistent calculation of band energies along lines connecting high-symmetry points  $K$ – $\Gamma$ – $M$ – $K$  (for definition, see Figure 1b). Various tests were performed to determine the optimal parameters in VASP. A  $k$ -point mesh of  $16 \times 16 \times 1$  points

**Table 2.** Geometrical Parameters (Distances in Å and Bond Angles in deg) for Chlorographene (CCl), Fluorographene (CF), and Graphane (CH) Obtained with PBE (Left Subcolumn) and HSE06 (Right Subcolumn) Functionals

System	$d(\text{C}-\text{C})$		$d(\text{C}-\text{X})$		$d(\text{X}-\text{X})$		$a(\text{C}-\text{C}-\text{C})$	
	PBE	HSE	PBE	HSE	PBE	HSE	PBE	HSE
CCl	1.76	1.74	1.79	1.73	2.91	2.88	111.51	111.99
CF	1.58	1.57	1.38	1.36	2.61	2.58	110.94	110.84
CH	1.54	1.53	1.10	1.10	2.54	2.52	111.63	111.54

including the  $\Gamma$  point was used to sample the Brillouin zone (BZ). This grid was reduced by VASP to 30 points with different weights  $w_k$  (defined such that they sum to 1) on the basis of the  $D_{3d}$  symmetry of the considered structures (Figure 1b). A cutoff energy of 500 eV was applied for the plane-wave basis set. As periodic boundary conditions were applied in all three dimensions, a vacuum layer of 30 Å was included to minimize any (spurious) interactions between adjacent layers.

In the GWA<sup>13</sup> calculations, usual Kohn–Sham equations were first solved

$$(T + V_{n-e} + V_H + V_{xc})\phi_{nk} = \phi_{nk} E_{nk} \quad (2)$$

where  $T$  is the kinetic-energy operator,  $V_{n-e}$  the potential of the nuclei,  $V_H$  the Hartree potential,  $V_{xc}$  the exchange–correlation energy, and  $n$  and  $k$  the band and  $k$ -point indices, respectively. Second, quasi-particle energies  $E_{nk}^{\text{QP}}$  within the GWA were calculated as a first-order correction to the DFT single-particle energies  $E_{nk}$

$$E_{nk}^{\text{QP},1} = \text{Re}[\langle \phi_{nk} | T + V_{n-e} + V_H + \sum_{\mathbf{c}} (G, W; E_{nk}) | \phi_{nk} \rangle] \quad (3)$$

that is, both Green's function  $G$  and the screened Coulomb interaction  $W$  in the self-energy operator  $\sum$  were calculated using the DFT single-particle energies and wave functions.<sup>35</sup> The corresponding single-shot total energy is henceforth referred to as  $G_0W_0$ . The updated quasiparticle energy  $E_{nk}^{\text{QP},i+1}$  was obtained from the quasiparticle energy at the previous iteration  $E_{nk}^{\text{QP},i}$

$$E_{nk}^{\text{QP},i+1} = E_{nk}^{\text{QP},i} + Z_{nk} \text{Re}[\langle \phi_{nk} | T + V_{n-e} + V_H + \sum_{\mathbf{c}} (G, W; E_{nk}^{\text{QP},i}) | \phi_{nk} \rangle - E_{nk}^{\text{QP},i}] \quad (4)$$

where  $Z_{nk}$  is the renormalization factor.<sup>35</sup> In the  $GW_0$  corrections, the screened Coulomb potential  $W$  was kept fixed at the initial DFT value ( $W_0$ ) and Green's function  $G$  was iterated. In the GW case,  $W$  and dielectric matrix were reevaluated in each iteration using the new quasi-particle energies. The iterative procedure is generally carried out until self-consistency is reached. In our case, we used four iterations to obtain well converged results. In addition, a default cutoff potential of 333.3 eV, 64 bands, and 192 frequency grid points were employed in the GW calculations. The ratio of relative computational costs is approximately 500:10:1 for our calculations using  $G_0W_0$ /HSE06/GGA functionals, respectively.

After the electronic ground states were determined, optical properties of the considered materials were investigated. The imaginary part of the macroscopic dielectric function  $\epsilon(\omega)$  was calculated in the long-wavelength limit ( $q \rightarrow 0$ ) by summation over the empty states<sup>36</sup>

$$\text{Im } \epsilon_{\alpha\beta}(\omega) = \frac{4\pi^2 e^2}{\Omega} \lim_{q \rightarrow 0} \frac{1}{q^2} \sum_{c,v,k} 2w_k \delta(\epsilon_{ck} - \epsilon_{vk} - \omega) \times \langle u_{ck+e,q} | u_{vk} \rangle \langle u_{ck+e,q} | u_{vk} \rangle^* \quad (5)$$

where the band indices  $c$  and  $v$  are restricted to the conduction and the valence band states, respectively ( $c_{\text{max}} + v_{\text{max}} = n_{\text{max}}$ ). The vectors  $e_\alpha$  are the unit vectors for the three Cartesian directions,  $\Omega$  is the volume of the unit cell, and commonly used notation  $\langle u_{n'k+q} | e^{iG} | u_{nk} \rangle = \langle \phi_{n'k+q} | e^{i(q+G)} | \phi_{nk} \rangle$  was adopted. Note that the frequency  $\omega$  has the dimension of an energy and  $\text{Im}\epsilon(\omega)$  was plotted for a light propagating along the CCl/CF/CH plane. Local field effects, that is, changes in the cell periodic part of the potential, were included in the random phase approximation (RPA). To show the physical origin of different features in the optical spectrum, we compared  $\text{Im}\epsilon$  calculated (i) without taking into account both e–e and e–h correlation, DFT+RPA,<sup>36</sup> (ii) with e–h interactions neglected, GW+RPA,<sup>35</sup> and finally, (iii) from the full solution of the Bethe–Salpeter equation<sup>23</sup> (BSE), which accounts for excitonic effects. The e–h excited state was represented by the expansion

$$|S\rangle = \sum_c^{\text{elec}} \sum_v^{\text{hole}} \sum_k A_{cvk}^S |cvk\rangle \quad (6)$$

where  $A^S$  is the amplitude of a free e–h pair configuration composed of the electron state  $|ck\rangle$  and the hole state  $|vk\rangle$ .  $A^S$  was obtained by diagonalization of the excitonic equation<sup>37,38</sup> implemented also in VASP,<sup>39</sup> according to eq 7, which corresponds to the BSE

$$(E_{ck}^{\text{QP}} - E_{vk}^{\text{QP}}) A_{cvk}^S + \sum_{c'v'k'} \langle cvk | K^{e-h} | c'v'k' \rangle A_{c'v'k'}^S = \Omega^S A_{cvk}^S \quad (7)$$

Where  $\Omega^S$  is the exciton excitation energy and  $K^{e-h}$  is the kernel describing the screened interaction between excited electrons and holes. Finally, BSE absorption spectra were obtained by calculating the imaginary part of the dielectric function.<sup>39</sup> Note that BSE was built on top of GWA. Therefore, corresponding spectra were referred to as  $G_0W_0$ +BSE, etc.

## RESULTS AND DISCUSSION

**DFT Calculations.** The lattice constants (Table 2,  $d(\text{X}-\text{X})$ ) obtained from GGA(PBE) optimization were slightly larger than those obtained using the HSE06 functional (the difference was 0.03, 0.03, and 0.02 Å for CCl, CF, and CH, respectively). The lattice constant and C–C distance in CCl (2.88 and 1.74 Å) were notably larger than the equivalent parameters for CF (2.58 and 1.57 Å) and CH (2.52 and 1.53 Å) and deviated from typical values for a single C(sp<sup>3</sup>)–C(sp<sup>3</sup>) bond ( $\sim 1.54$  Å). This is because chlorine atoms attached to the perturbed graphene sp<sup>3</sup> lattice partially overlap with each other and the whole lattice must balance C–C bonding with Cl–Cl repulsion. Notice also decreasing electron density in the middle of the C–X and C–C



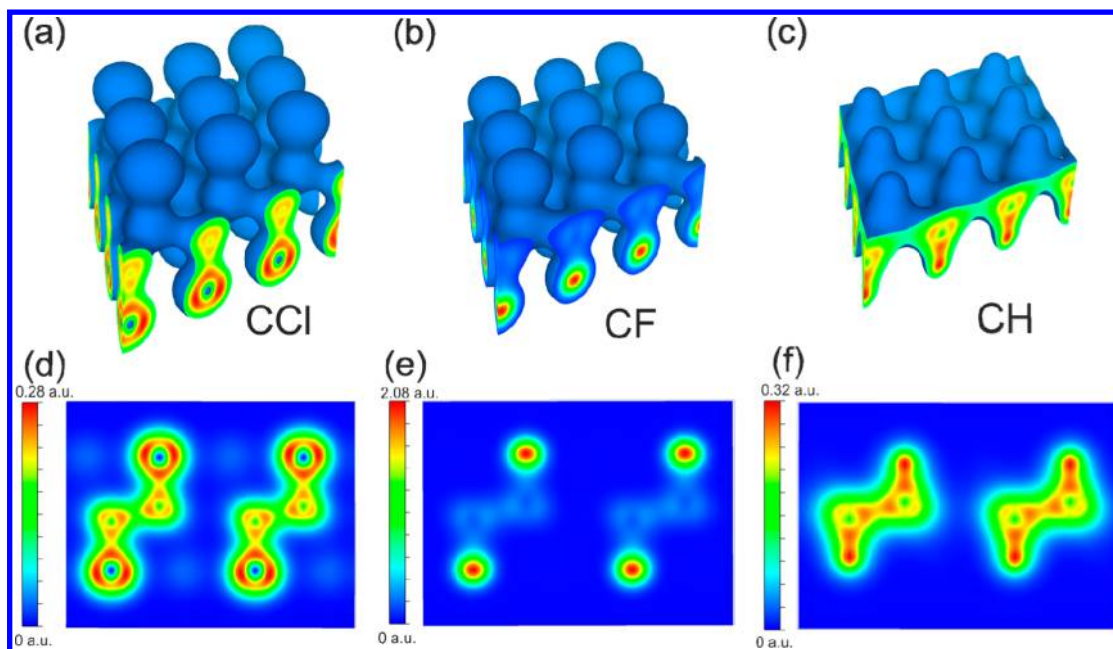


**Figure 2.** Total electron densities for chlorographene (CCI) (a,d), fluorographene (CF) (b,e) and graphane (CH) (c,f) calculated using the HSE06 functional. (a–c) Isosurfaces for isovalues of 0.1 au plotted for a  $3 \times 3$  supercell. (d–f) Electron density cuts through the (110) plane (see Figure 1c) for a  $2 \times 2$  supercell.

bonds with increasing size of the halogen/hydrogen atom (Figure 2). Consequently, CCI was predicted to be less stable than CH and CF,<sup>22</sup> and from an experimental point of view, CCI is likely to be unstable under ambient conditions. The pristine parent material (graphite chloride) has been shown to be unstable at temperatures  $>0^\circ\text{C}$  but stable at lower temperatures.<sup>40</sup> However, nonstoichiometric graphene chloride with low concentrations of approximately 8 or 30 at. % Cl has recently been prepared<sup>9,10</sup> and its stability confirmed from room temperature to  $500^\circ\text{C}$ .

The CCI band gap of 1.41 eV obtained using the PBE functional indicates it has semiconducting or insulating properties. Surprisingly, fully chlorinated graphene, CCI, has scarcely been mentioned in the literature and the first theoretical remark<sup>14</sup> suggested it exhibits metallic behavior. This probably stemmed from the formation of “nonbonded” structures (composed of carbon  $\text{sp}^2$  networks and very weakly bound chlorine atoms) reported later,<sup>41</sup> as confirmed recently in a study of the reaction mechanism between Cl atoms and graphene,<sup>42</sup> or alternatively, Cl atom adsorption.<sup>43,44</sup> In contrast, our PBE band gaps of CH and CF (3.53 and 3.09 eV) were in agreement with values reported earlier (see, e.g., ref 22 and references therein). CCI is much more polarizable than CF due to the chlorine substituents, hence the band gap is smaller. On the other hand, CF is rather ionic in character (Bader analysis suggested charge transfer of  $\sim 0.6$  e from C to F in CF versus  $\sim 0.1$  e from C to Cl in CCI), therefore the band gap opens. The corresponding dielectric constants confirm this (see Supporting Information). The HSE06 functional gave notably larger band gaps than the PBE functional (Table 3; see also refs 22 and 45). The difference was 1.40 eV, 1.84 and 0.85 eV for CCI, CF and CH, respectively. The inclusion of some fraction of exact HF exchange not only led to a systematic increase in calculated band gaps but also changed the trend in band gaps; the HSE06 functional predicted  $E_g(\text{CF}) > E_g(\text{CH}) > E_g(\text{CCI})$  in agreement with GWA (see below), whereas for PBE band gaps,  $E_g(\text{CH}) > E_g(\text{CF}) > E_g(\text{CCI})$ .

**Table 3.** Band gaps of chlorographene (CCI), fluorographene (CF) and graphane (CH) in eV

System	CCI		CF <sup>a</sup>		CH	
Method/orbitals	PBE	HSE06	PBE	HSE06	PBE	HSE06
DFT	1.41	2.81	3.09	4.93	3.53	4.38
$G_0W_0$	4.07	4.54	6.98	7.69	5.64	5.83
$GW_0$	4.46	4.73	7.48	7.95	5.89	5.95
GW	4.89	4.93	8.12	8.28	6.28	6.17

<sup>a</sup>Experimental band gap  $>3$  eV or  $>3.8$  eV, see Table 1

**Calculations using the GW approximation.** In our calculations based on many-body GW theory, band gap values were found to be sensitive to many parameters, such as k-point sampling of BZ, cutoff energy, thickness of vacuum layer, number of bands included and frequency grid. For example, for CH, we obtained larger  $G_0W_0$ -PBE and  $GW_0$ -PBE band gaps of 5.9 and 6.2 eV, respectively, for a sparse frequency grid (48 points) compared to band gaps of 5.7 and 5.9 eV, respectively, for a frequency grid of 96 points (other parameters being identical); similar values to the latter were obtained with a denser grid (144 points). In a similar way, we tested other parameters, e.g., a GW band gap error of about 0.6 and 0.1 eV was introduced when the sampling of BZ was changed from  $16 \times 16 \times 1 \rightarrow 4 \times 4 \times 1$  and  $16 \times 16 \times 1 \rightarrow 10 \times 10 \times 1$ , respectively. Simultaneous tests of several parameters showed that the band gaps predicted by the many-body GW theory converged to within 0.02 eV. Finally, the predicted CH band gap values (5.64 and 5.89 eV for  $G_0W_0$ -PBE and  $GW_0$ -PBE, respectively; Table 3) were in reasonable agreement with values reported in the literature, i.e., 5.4 eV<sup>19</sup> ( $G_0W_0$ -LDA), 5.7 eV<sup>14</sup> ( $G_0W_0$ -LDA), 5.4 eV<sup>20</sup> ( $G_0W_0$ -LDA), 5.7 eV<sup>21</sup> ( $G_0W_0$ -GGA), 6.1 eV<sup>15</sup> ( $G_0W_0$ -GGA), 6.1 eV<sup>46</sup> ( $G_0W_0$ -LDA) and 6.0 eV<sup>17</sup> ( $GW_0$ -LDA). However, the variation in literature values is understandable considering the different conditions used, e.g., use of pseudopotentials or PAW method and different software (VASP, Abinit+Yambo, Quantum Espresso), and sensitivity to

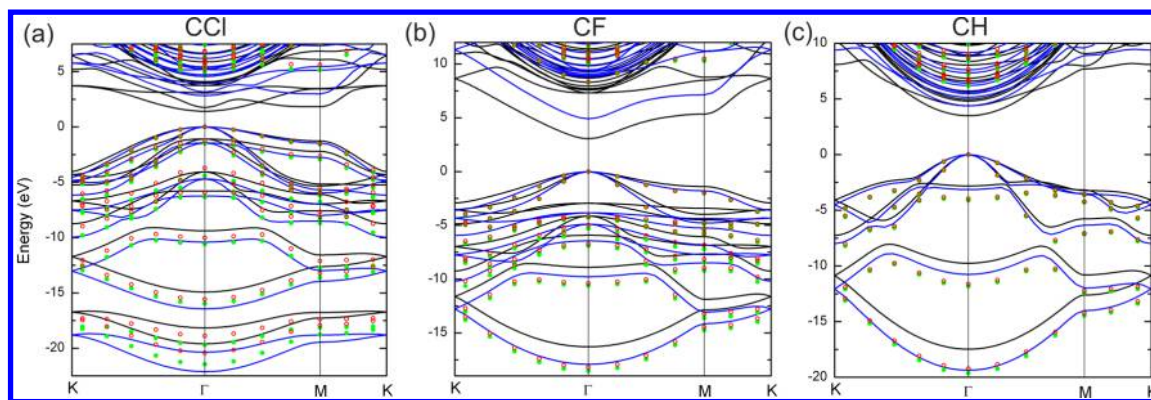


**Figure 3.** The electronic band structure in the vicinity of the band gap for chlorographene (a), fluorographene (b), and graphane (c) along lines connecting the high symmetry points K,  $\Gamma$ , and M in the Brillouin zone (for definitions, see Figure 1). Band structures were calculated using the PBE functional (black line), HSE06 functional (blue line), GW over PBE (red circles) and GW over HSE06 (green dots). The Fermi level was set at zero energy.

the aforementioned parameters. In addition, the level of approximation used in calculations of band gaps based on the many-body GW theory is sometimes not precisely documented in the literature, e.g.,  $G_0W_0$  and  $GW_0$  calculations are often generally labeled as GW. For CF, our  $G_0W_0$ -PBE and  $GW_0$ -PBE band gap values of 7.0 and 7.5 eV flank band gap values reported in the literature: 7.4 eV<sup>14</sup> ( $G_0W_0$ -LDA), 7.4 eV<sup>15</sup> ( $G_0W_0$ -GGA), 7.5 eV<sup>18</sup> ( $G_0W_0$ -GGA), 7.3 eV<sup>16</sup> ( $G_0W_0$ -LDA) and 7.49 eV<sup>17</sup> ( $GW_0$ -LDA). Again, small differences or apparent similarities between the literature values can be attributed to the different methods, parameters and software used. Our  $GW_0$ -PBE band gap value of 4.46 eV for CCl agrees well with the only literature value of 4.33 eV<sup>47</sup> ( $GW_0$ -LDA).

Whereas the HSE06 functional gave notably larger band gaps than the PBE functional (as discussed above), differences between bands gap from GWA constructed over HSE06 and PBE orbitals were smaller (Table 3).  $G_0W_0$ -HSE06 band gaps were larger by 0.47 eV, 0.71 and 0.19 eV (for CCl, CF and CH, respectively) than  $G_0W_0$ -PBE band gaps, whereas  $GW_0$ -HSE06 band gaps exhibited smaller differences of 0.27 eV, 0.47 and 0.06 eV, respectively, with respect to  $GW_0$ -PBE band gaps. At the highest level of theory,  $GW$ -HSE06 gave almost same values as  $GW$ -PBE (i.e., differences 0.04 eV, 0.016 eV,  $-0.11$  eV for CCl, CF and CH, respectively). The predicted energy-band structure was different for the DFT and GWA calculations. However, further analysis suggested that the general shape of individual bands was rather similar but distances between individual bands were different. Surprisingly, similar trends were observed when comparing band structures from calculations with different DFT orbitals, i.e., HSE06 vs PBE,  $G_0W_0$ -HSE06 vs  $G_0W_0$ -PBE, etc. A comparison of the band structures for CCl, CF, and CH is shown in Figure 3. Simplistically, band structures could be related by multiplying the energies of occupied states by one coefficient and the energies of unoccupied states by a different coefficient. All compounds considered here were predicted to be direct band gap materials. The bottom of the conduction band and top of the valence band are located at the  $\Gamma$  point in the first Brillouin zone and the maximum band gap is located at the K point. The top of the valence band is doubly degenerate, belongs to the  $E_g$  irreducible representation and has  $p_{xy}$  character (from C and Cl or F atom; from C only for CH). The bottom of the (nondegenerate) conduction-band has  $p_z$  character and belongs to the  $A_{2u}$  irreducible representation.

Furthermore, the effects of different degrees of self-consistency in GWA ( $G_0W_0$ ,  $GW_0$  and  $GW$ ) were investigated. For 3D materials, there is consensus that GWA systematically improves the band gap of semiconductors and insulators; calculated single shot  $G_0W_0$  band gaps are often within 10% of experimental values (typically underestimated) and the best agreement with experiment is achieved by  $GW_0$  (see, e.g., ref 48; most calculations have considered LDA or GGA orbitals) because GW band gaps are sometimes slightly overestimated. Nevertheless, we observed some trends in the calculated values notwithstanding the differences from experimental values. Large differences in band gaps due to differing degrees of self-consistency occurred in the case of the calculations with PBE orbitals. In particular, for CCl and CF, there was a shift of about 1 eV between the  $G_0W_0$ -PBE and  $GW$ -PBE band gap (Table 3). Whereas this was apparent for PBE orbitals, the calculations with more realistic HSE06 orbitals were more consistent, i.e., there was only a slight difference between the  $G_0W_0$ -HSE06 and  $GW$ -HSE06 values (Table 3). Application of HSE06 orbitals as a zero order description for GWA calculations has been recommended for 3D materials (also if the PBE band gap is inverted or too small, HSE screening properties are preferable).<sup>32</sup> Finally, the results suggested that in predicting the band gaps of CCl, CF and CH, a similar accuracy could be achieved by  $G_0W_0$ -HSE06 as by  $GW_0$ -PBE (Table 3). However,  $G_0W_0$ -HSE06 is computationally less demanding since several iterations are required to converge  $G$  in the  $GW_0$ -PBE approach. Our findings agree with the general trends observed in a previous study, in which  $GW_0$ -PBE and  $G_0W_0$ -HSE06 approaches were applied to model 3D materials.<sup>32</sup>

**Optical properties.** In the case of insulating CF, GWA band gaps ( $\sim 8$  eV) were significantly different from the experimentally observed absorption peaks (at 3 or 3.8 eV). A large overestimation of band gap using GWA has also been reported for a  $\text{MoS}_2$  monolayer (PBE 1.6 eV  $\rightarrow$   $GW_0$ -PBE 2.5 eV; exp. on bulk  $\text{MoS}_2$  gives gap 1.7–1.8 eV)<sup>49</sup> and this casts doubt on whether GWA is suitable for 2D structures. However, calculated electronic band gaps and energies of electron transitions derived from optical spectra do not match exactly because the electron transitions observed in optical spectra involve formation of an exciton. Therefore, DFT and GW band gaps should not be directly compared with optical spectra. We calculated optical spectra by using the BSE method including

excitonic effects and compared positions of the first absorption peaks with available experimental data (*cf.* Table 1).

The theoretical absorption spectra directly correspond to the imaginary part of the dielectric function,  $\text{Im}\epsilon(\omega)$ . From a technical viewpoint, optical transition simulation requires integration over the irreducible Brillouin zone using a sufficiently dense  $k$ -point mesh. Naturally, the convergence of  $k$ -point sampling is important. The optical absorption spectra for light polarization parallel to the surface plane obtained with different  $k$ -point meshes using  $G_0W_0(\text{PBE})+\text{BSE}$  are illustrated in Figure 4a for CF. The three absorption peaks with the lowest

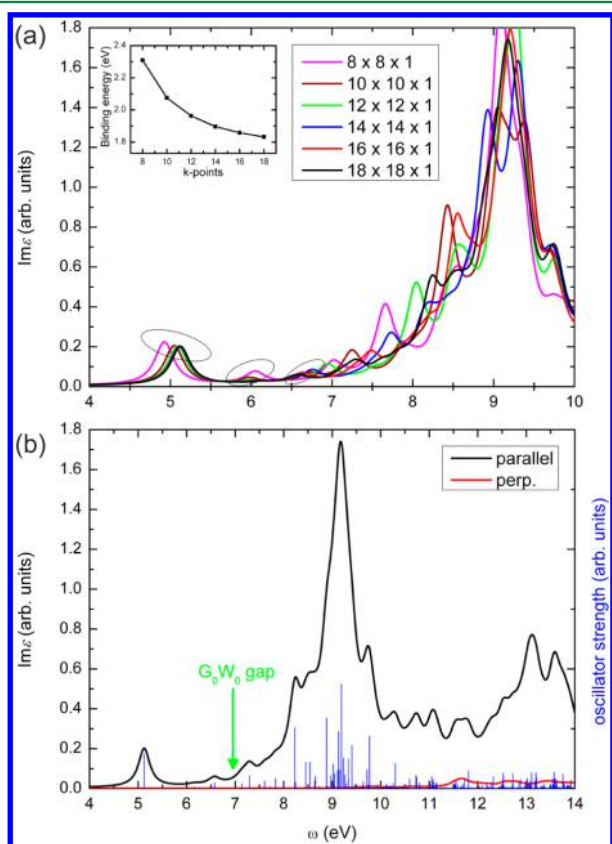


**Figure 4.**  $G_0W_0(\text{PBE})+\text{BSE}$  absorption spectra of fluorographene (CF) for light polarization parallel to the surface plane (a) obtained using different  $k$ -point meshes. Inset: convergence of the binding energy of the first optically active exciton (b) compared with absorption spectra of CF for light polarization perpendicular to the surface plane (red line). Oscillator strengths for all transitions are shown as blue columns.

energy (at about 5.1 eV, 6.1 and 6.6 eV; highlighted in Figure 4a), originating from bound excitons were found to converged with an  $18 \times 18 \times 1$   $k$ -point grid. As  $k$  was increased, an increasing number of optically active bound excitons became evident (from 6 to 12 excitons in Figure 4a) and their binding energy converged within 0.02 eV (for convergence of the binding energy of the first optically active exciton see inset of Figure 4a). However, the dominant peak at 9–10 eV was still not converged sufficiently with an  $18 \times 18 \times 1$  grid; previous calculations have suggested that very dense grids are necessary to obtain converged spectra for the 0–20 eV frequency window ( $30 \times 30 \times 1^{20}$  or  $40 \times 40 \times 1^{16}$ ). Because the number of  $k$  points directly relates to the rank of the BSE Hamiltonian, causing extreme demands in terms of storage and CPU time for

the calculation of the spectra, we decided to use  $18 \times 18 \times 1$   $k$ -point grid and 192 frequency grid for evaluation of  $e$ – $h$  kernel in the BSE and the dielectric function (the important first exciton peak was well converged). In addition, we included all valence (11 for CCl and CF, 5 for CH) and 13 conduction bands (maximal  $v$  and  $c$  indices in eqs 6 and 7) to obtain  $\epsilon(\omega)$  at  $\text{GW}+\text{BSE}$  level as we were only interested in the low energy region of the spectrum.

We noted that the optical absorption spectrum for light polarization perpendicular to the surface plane was almost negligible up to 11 eV, as shown in Figure 4b. This indicates that CF exhibits strong optical anisotropy because completely different absorption spectra were obtained for light polarization parallel to the surface plane. Similar is valid for CCl and CH (data not shown). It is worth noting that the same behavior was reported for CH and CF in previous works (ref 20 for CH and ref 50 for CF). Optical anisotropy of CH, CF, and CCl is induced by changes in the cell periodic part of the potential (local-field effects) and, in addition, for CH there are low energy excitons (see below) visible for the parallel polarization but dipole forbidden for the perpendicular polarization.<sup>20</sup> The first exciton peak of CF for light polarization parallel to the surface plane was found to be located at 5.1 eV ( $G_0W_0(\text{PBE})+\text{BSE}$ ), substantially lower than the corresponding  $G_0W_0(\text{PBE})$  band gap value at 7.0 eV (green arrow in Figure 4b). This difference corresponds to an exciton with a large binding energy of 1.9 eV. To understand the origin of the absorption peaks, we examined the oscillator strengths of the excitonic transitions contributing to the absorption spectrum in that region. We carried out a series of calculations that included only selected valence and conduction bands. Only vertical transitions from the two highest occupied bands to the lowest empty band were found to be responsible for the exciton peaks of bound excitons (indicated in Figure 4a by ovals). Major transitions contributing to the dominant absorption peak at 9.2 eV originated from the two highest occupied bands and the four lowest empty bands. The computation of oscillator strengths (Figure 4b) included 11 valence and 13 conduction bands.

Electron–hole excitations, which are not included in GW itself, were clearly responsible for the optical absorption at energies lower than GW band gaps. This is demonstrated in Figures 5a, 5b, and 5c for CCl, CF, and CH, respectively, where optical spectra calculated by (i)  $\text{PBE}+\text{RPA}$  ( $e$ – $e$  and  $e$ – $h$  correlation neglected), (ii)  $G_0W_0(\text{PBE})+\text{RPA}$  ( $e$ – $e$  correlation included and  $e$ – $h$  correlation neglected), and (iii)  $G_0W_0(\text{PBE})+\text{BSE}$  (accounts both for  $e$ – $e$  and  $e$ – $h$  effects) are presented. Comparison of the optical absorption spectra obtained at the  $\text{DFT}+\text{RPA}$  and  $G_0W_0+\text{RPA}$  levels shows that inclusion of  $e$ – $e$  interaction led to a blue shift due to quasi particle corrections. However, the shape of the spectra was preserved. On the other hand, inclusion of  $e$ – $h$  attraction yielded a significant red shift of the absorption spectrum (insets in Figure 5). Furthermore, redistribution of the spectral weight to lower photon energies was observed. A number of pronounced excitonic resonances also appeared. The most prominent physical effect of the  $e$ – $h$  interactions was appearance of some bound excitons below the  $G_0W_0$  gap (see insets in Figure 5), which were completely missing in the  $G_0W_0+\text{RPA}$ . In the case of CCl, two low energy peaks were evident at 2.82 and 3.33 eV and a shoulder at 3.86 eV (corresponding to the resonant peak at 4.18 eV) due to bound excitons. The binding energy of the exciton with the lowest



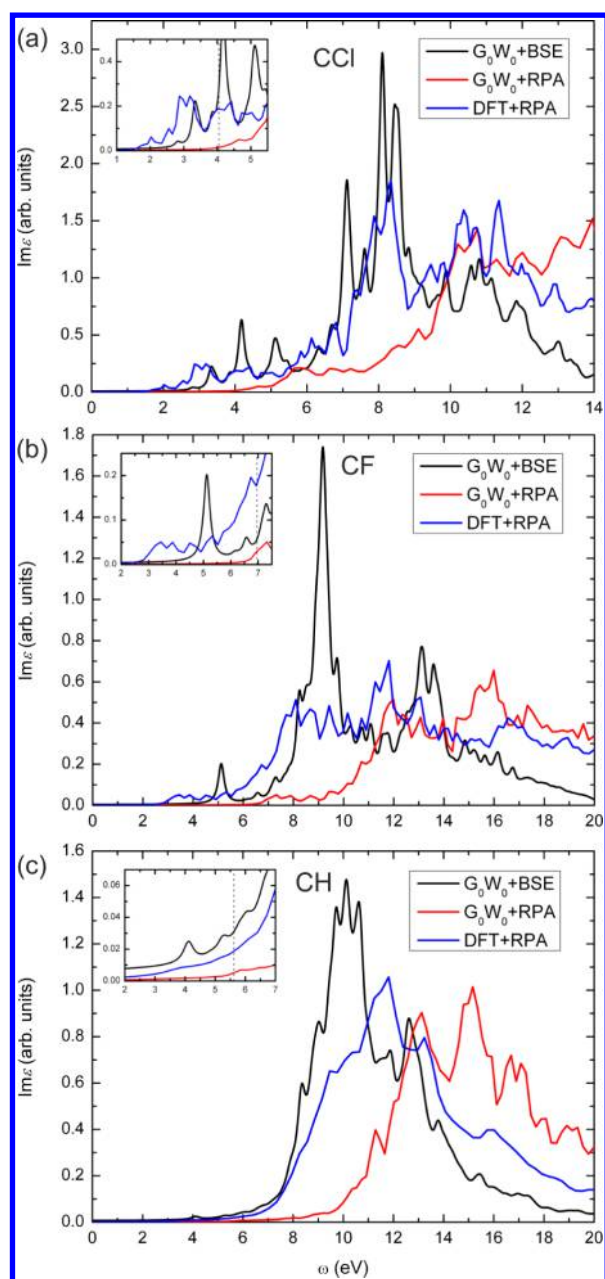


**Figure 5.** Absorption spectra of (a) CCl, (b) CF, and (c) CH for light polarization parallel to the surface plane. Insets show amplified regions of the absorption spectra in the vicinity of the first exciton peak and  $G_0W_0(\text{PBE})$  gap (dashed line).

energy was 1.25 eV. For CF, there were low energy peaks at 5.12 and 6.58 eV with a shoulder at 6.23 eV, and the lowest energy exciton had a binding energy of 1.85 eV. The presented values are shifted to lower energies with respect to values reported in ref 18 (peaks at 5.4 and 7.2 eV,  $G_0W_0$  gap at 7.5 eV). The lowest energy of a bound exciton in CH was 4.11 eV and had a binding energy of 1.53 eV, in agreement with ref 20 (binding energy of 1.6 eV), with the second peak located at 5.30 eV. The discussed exciton energies suggest that CF and CH exhibit UV absorption, whereas CCl displays visible light absorption.

For the sake of completeness, it should be noted that the effect of using different degrees of self-consistency in GWA on top of PBE and HSE06 orbitals on the first exciton peak

roughly corresponded to the effect on GWA band gap discussed above. The same order of GW gaps and absorption peaks was preserved, as shown in Figure 6. The first exciton

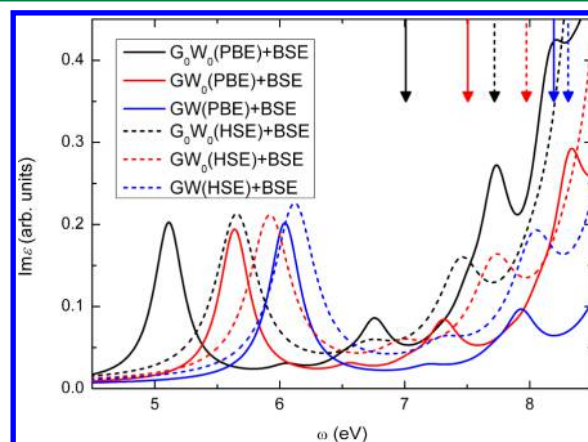


**Figure 6.** The first exciton peak of the CF absorption spectra obtained using different degrees of self-consistency in GWA on top of PBE and HSE06 orbitals calculated using a  $14 \times 14 \times 1$  k-point grid. Corresponding band gap values are shown as arrows.

peak was on average shifted by  $\sim 2$  eV to lower energies with respect to the corresponding band gap value from GWA. To summarize this part, consideration of e–h interactions is crucial for predicting absorption spectra of CCl, CF and CH that are directly comparable with experimental optical spectra. There is a large cancellation of e–e and e–h effects. This explains why the experimental absorption value ( $>3.8$  eV) is significantly red-shifted with respect to GW band gaps (7–8 eV), whereas the PBE band gap values fortuitously agree with this experimental value.

**Role of defects.** The experimentally prepared materials may contain some (usually small) amount of various defects, which may influence the electronic structure and behavior of the respective material. Therefore, we analyzed the role of point defects on the electronic structure of the considered graphene derivatives. It is worth noting that the presence of defects in CF has been suggested as a possible explanation for the discrepancy between experimental values and GWA band gaps.<sup>15,18,51</sup> However, various conformations (chair, boat, zigzag and armchair) for both CF and CH have been shown to have similar band gaps on both DFT and GW levels.<sup>15,18,52,53</sup> Here, we focused on selected point defects.

We investigated four types of point defects (Figure 7 for CF): (i) Stone–Wales (SW) defect, (ii) Cl/F/H vacancy, (iii) C vacancy, and (iv) interstitial Cl/F/H located at the site of a C vacancy. SW defect is the simplest example of the graphene lattice reconstruction by forming nonhexagonal rings:<sup>54</sup> four hexagons are transformed into two pentagons and two heptagons [SW(55–77) defect] by rotating one of the C–C bonds by  $90^\circ$  (Figure 7a). We used a  $3 \times 3$  supercell (with 36 or 35 atoms) and  $5 \times 5 \times 1$  k-point sampling for optimization of atomic position in a fixed supercell at PBE level. The density of states (DOS) and imaginary part of the dielectric function,  $\text{Im}\epsilon(\omega)$ , were obtained for a  $7 \times 7 \times 1$  k-point grid. The independent-particle (IP) picture was adopted within DFT (DFT-IP) for  $\text{Im}\epsilon(\omega)$  and no local field effect was included at RPA level. We checked in the case of CF that the DFT-IP and DFT+RPA spectra did not differ substantially, especially in the low-energy region.

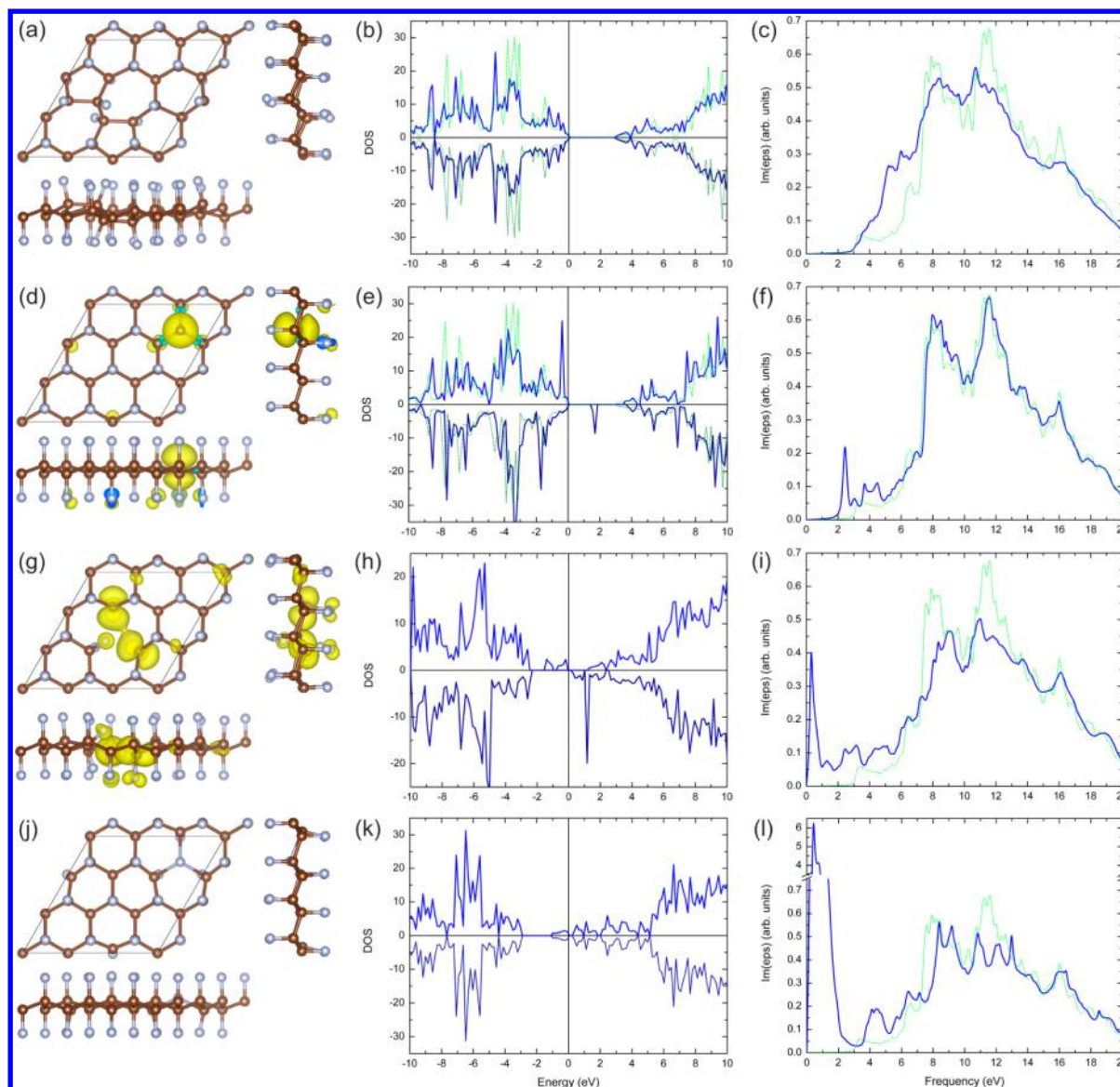


**Figure 7.** Geometrical structures, density of states (DOS) and optical absorption spectra for light polarization parallel to the surface plane of defective fluorographenes. Stone-Wales defect (a–c), F vacancy (d–f), C vacancy (g–i), and interstitial F (j–l) were considered. DOS and spectra for virgin CF are also shown for comparison (green dotted line). For DOS, the Fermi level was set to zero. Spin densities are added to plots containing geometrical structures.

Stone–Wales defects (Figure 7a–c) did not affect the band gap of CF, as seen from DOS plot, and the corresponding absorption spectrum of defective CF was similar to pure CF. The total magnetization equaled to zero, that is, the system was nonspin-polarized (closed shell). The DOS and absorption spectrum of the system with fluorine vacancies were very similar to those of virgin CF (Figure 7d–f). However, peaks corresponding to a dangling bond were evident in the DOS plot. In the limit of a low density of defects (large supercell), such peaks in DOS would be reduced to lines, and therefore, the band gap would remain again rather unaffected. Spin density (difference between  $\alpha$  and  $\beta$  electron density, Figure 7d) was located in the vicinity of an unpaired carbon atom, below and above the CF plane. On the other hand, C vacancies led to a double fluorinated carbon atom, two carbon dangling bonds and substantial shift of Fermi level. The original band gap of  $\sim 3$  eV was significantly perturbed by these features, which implies a broad peak in the visible light region of the

absorption spectra (Figure 7g–i). Spin density was located in the vicinity of carbon atoms with unpaired electrons, here in the CF plane. The final considered defect, interstitial F located at the site of a C vacancy, led to substantial changes in the DOS. This is a typical feature of n-type semiconductors, that is, there are valence and dopant bands below the Fermi level. A broad peak located at 0.4 eV appeared in the absorption spectra. It is worth noting, that the last type of defect is not very stable with respect to the preceding ones. Taking into account, the rather low concentration of defects in 2D graphene derivatives (here CF, CCl, and CH), we concluded that point defects may lead to slight lowering of band gaps.

## CONCLUSIONS

The many-body GW approximation is often considered a “benchmark” method against which other methods are assessed. However, so far there has been no systematic study of the effects of using various levels of GWA on the predicted



band gap values of the recently developed 2D carbon-based materials (e.g., chlorographene, fluorographene, and graphane). Here, we presented values of many-body GWA band gaps computed at  $G_0W_0$ ,  $GW_0$ , and GW levels constructed over GGA (PBE) and hybrid (HSE06) orbitals. Whereas DFT calculations at HSE06 level gave notably larger band gaps than calculations at PBE level, the GWA calculations over HSE06 orbitals gave similar band gaps to GWA over PBE. The band gap of CCl (4.93 eV at the highest GW-HSE06 level) was predicted to be smaller than that of CH (6.17 eV) or CF (8.28 eV). However, CCl can still be considered a wide-band gap insulator analogous to CF and CH. The optical properties of the considered materials were investigated at BSE+GW level and the inclusion of electron–hole interaction was found to be crucial for predicting low energy absorption peaks of excitonic nature. The formation of exciton peaks at 2.82, 5.12, and 4.11 eV with huge binding energy of 1.25, 1.85, and 1.53 eV for CCl, CF, and CH, respectively, was observed. The large binding energy of an exciton in CF can also explain the putative discrepancy between the GW band gap (7–8 eV) and the experimental observations (>3 or >3.8 eV). The role of point defects was predicted to be synergistic but is likely to be small considering the low concentration of defects in real materials.

## ■ ASSOCIATED CONTENT

### ■ Supporting Information

Outputs from Bader analysis, macroscopic static dielectric tensors, and basic information about computational cost. This information is available free of charge via the Internet at <http://pubs.acs.org/>.

## ■ AUTHOR INFORMATION

### Corresponding Author

\*E-mail: [frantisek.karlicky@upol.cz](mailto:frantisek.karlicky@upol.cz) (F.K.); [michal.otyepka@upol.cz](mailto:michal.otyepka@upol.cz) (M.O.).

### Notes

The authors declare no competing financial interest.

## ■ ACKNOWLEDGMENTS

Financial support from the Czech Science Foundation (P208/12/G016), the Operational Program Research and Development for Innovations—European Regional Development Fund (project CZ.1.05/2.1.00/03.0058 of the Ministry of Education, Youth and Sports of the Czech Republic), the Barrande project (No. 7AMB12FR026) and the Operational Program Education for Competitiveness—European Social Fund (project CZ.1.07/2.3.00/20.0017 of the Ministry of Education, Youth and Sports of the Czech Republic) is gratefully acknowledged.

## ■ REFERENCES

- (1) Georgakilas, V.; Otyepka, M.; Bourlinos, A. B.; Chandra, V.; Kim, N.; Kemp, K. C.; Hobza, P.; Zboril, R.; Kim, K. S. Functionalization of Graphene: Covalent and Non-Covalent Approaches, Derivatives and Applications. *Chem. Rev.* **2012**, *112*, 6156–6214.
- (2) Karlický, F.; Datta, K. K. R.; Otyepka, M.; Zbořil, R. Halogenated Graphenes: Rapidly Growing Family of Graphene Derivatives. *ACS Nano* **2013**, DOI: 10.1021/nn4024027.
- (3) Sluiter, M. H. F.; Kawazoe, Y. Cluster Expansion Method for Adsorption: Application to Hydrogen Chemisorption on Graphene. *Phys. Rev. B* **2003**, *68*, 085410.
- (4) Sofo, J. O.; Chaudhari, A. S.; Barber, G. D. Graphane: A Two-Dimensional Hydrocarbon. *Phys. Rev. B* **2007**, *75*, 153401.
- (5) Elias, D. C.; Nair, R. R.; Mohiuddin, T. M. G.; Morozov, S. V.; Blake, P.; Halsall, M. P.; Ferrari, A. C.; Boukhvalov, D. W.; Katsnelson, M. I.; Geim, A. K.; Novoselov, K. S. Control of Graphene's Properties by Reversible Hydrogenation: Evidence for Graphane. *Science* **2009**, *323*, 610–613.
- (6) Ryu, S.; Han, M. Y.; Maultzsch, J.; Heinz, T. F.; Kim, P.; Steigerwald, M. L.; Brus, L. E. Reversible Basal Plane Hydrogenation of Graphene. *Nano Lett.* **2008**, *8*, 4597–4602.
- (7) Nair, R. R.; Ren, W. C.; Jalil, R.; Riaz, I.; Kravets, V. G.; Britnell, L.; Blake, P.; Schedin, F.; Mayorov, A. S.; Yuan, S. J.; Katsnelson, M. I.; Cheng, H.-M.; Strupinski, W.; Bulusheva, L. G.; Okotrub, A. V.; Grigorieva, I. V.; Grigorenko, A. N.; Novoselov, K. S.; Geim, A. K. Fluorographene: A Two-Dimensional Counterpart of Teflon. *Small* **2010**, *6*, 2877–2884.
- (8) Zbořil, R.; Karlický, F.; Bourlinos, A. B.; Steriotis, T. A.; Stubos, A. K.; Georgakilas, V.; Šafářová, K.; Jančík, D.; Trapalis, C.; Otyepka, M. Graphene Fluoride: A Stable Stoichiometric Graphene Derivative and its Chemical Conversion to Graphene. *Small* **2010**, *6*, 2885–2891.
- (9) Li, B.; Zhou, L.; Wu, D.; Peng, H. L.; Yan, K.; Zhou, Y.; Liu, Z. F. Photochemical Chlorination of Graphene. *ACS Nano* **2011**, *5*, 5957–5961.
- (10) Gopalakrishnan, K.; Subrahmanyam, K. S.; Kumar, P.; Govindaraj, A.; Rao, C. N. R. Reversible Chemical Storage of Halogens in Few-Layer Graphene. *RSC Adv.* **2012**, *2*, 1605–1608.
- (11) Liu, C.; Li, Y.; Lee, M. V.; Kumatani, A.; Tsukagoshi, K. Self-Assembly of Semiconductor/Insulator Interfaces in One-Step Spin-Coating—A Versatile Approach for Organic Field-Effect Transistors. *Phys. Chem. Chem. Phys.* **2013**, *15*, 7917–7933.
- (12) Song, W.; Ji, X.; Deng, W.; Chen, Q.; Shena, C.; Banks, C. E. Graphene Ultracapacitors: Structural Impacts. *Phys. Chem. Chem. Phys.* **2013**, *15*, 4799–4803.
- (13) Hedin, L. New Method for Calculating 1-Particle Greens Function with Application to Electron-Gas Problem. *Phys. Rev.* **1965**, *139*, A796–A823.
- (14) Klintonberg, M.; Lebegue, S.; Katsnelson, M. I.; Eriksson, O. Theoretical Analysis of the Chemical Bonding and Electronic Structure of Graphene Interacting with Group IA and Group VIIA Elements. *Phys. Rev. B* **2010**, *81*, 085433.
- (15) Leenaerts, O.; Peelaers, H.; Hernandez-Nieves, A. D.; Partoens, B.; Peeters, F. M. First-Principles Investigation of Graphene Fluoride and Graphane. *Phys. Rev. B* **2010**, *82*, 195436.
- (16) Liang, Y.; Yang, L. Electronic Structure and Optical Absorption of Fluorographene. *MRS Proc.* **2011**, *1370*, 137.
- (17) Sahin, H.; Topsakal, M.; Ciraci, S. Structures of Fluorinated Graphene and Their Signatures. *Phys. Rev. B* **2011**, *83*, 115432.
- (18) Samarakoon, D. K.; Chen, Z. F.; Nicolas, C.; Wang, X. Q. Structural and Electronic Properties of Fluorographene. *Small* **2011**, *7*, 965–969.
- (19) Lebegue, S.; Klintonberg, M.; Eriksson, O.; Katsnelson, M. I. Accurate Electronic Band Gap of Pure and Functionalized Graphene from GW Calculations. *Phys. Rev. B* **2009**, *79*, 245117.
- (20) Cudazzo, P.; Attaccalite, C.; Tokatly, I. V.; Rubio, A. Strong Charge-Transfer Excitonic Effects and the Bose-Einstein Exciton Condensate in Graphane. *Phys. Rev. Lett.* **2010**, *104*, 226804.
- (21) Pulci, O.; Gori, P.; Marsili, M.; Garbuio, V.; Seitsonen, A. P.; Bechstedt, F.; Cricenti, A.; Del Sole, R. Electronic and Optical Properties of Group IV Two-Dimensional Materials. *Phys. Status Solidi A* **2010**, *207*, 291–299.
- (22) Karlický, F.; Zbořil, R.; Otyepka, M. Band Gaps and Structural Properties of Graphene Halides and Their Derivates: A Hybrid Functional Study with Localized Orbital Basis Sets. *J. Chem. Phys.* **2012**, *137*, 034709.
- (23) Bethe, H. A.; Salpeter, E. E. A Relativistic Equation for Bound State Problems. *Phys. Rev.* **1951**, *82*, 309–310.
- (24) Onida, G.; Reining, L.; Rubio, A. Electronic Excitations: Density-Functional versus Many-Body Green's-Function Approaches. *Rev. Mod. Phys.* **2002**, *74*, 601–659.

- (25) Heyd, J.; Scuseria, G. E.; Ernzerhof, M. Hybrid Functionals Based on a Screened Coulomb Potential. *J. Chem. Phys.* **2003**, *118*, 8207–8215.
- (26) Krukau, A. V.; Vydrov, O. A.; Izmaylov, A. F.; Scuseria, G. E. Influence of the Exchange Screening Parameter on the Performance of Screened Hybrid Functionals. *J. Chem. Phys.* **2006**, *125*, 224106.
- (27) Jeon, K. J.; Lee, Z.; Pollak, E.; Moreschini, L.; Bostwick, A.; Park, C. M.; Mendelsberg, R.; Radmilovic, V.; Kostecki, R.; Richardson, T. J.; Rotenberg, E. Fluorographene: A Wide Bandgap Semiconductor with Ultraviolet Luminescence. *ACS Nano* **2011**, *5*, 1042–1046.
- (28) Wang, Z. F.; Wang, J. Q.; Li, Z. P.; Gong, P. W.; Liu, X. H.; Zhang, L. B.; Ren, J. F.; Wang, H. G.; Yang, S. R. Synthesis of Fluorinated Graphene with Tunable Degree of Fluorination. *Carbon* **2012**, *50*, 5403–5410.
- (29) Kummel, S.; Kronik, L. Orbital-Dependent Density Functionals: Theory and Applications. *Rev. Mod. Phys.* **2008**, *80*, 3–60.
- (30) Heyd, J.; Scuseria, G. E. Efficient Hybrid Density Functional Calculations in Solids: Assessment of the Heyd-Scuseria-Ernzerhof Screened Coulomb Hybrid Functional. *J. Chem. Phys.* **2004**, *121*, 1187–1192.
- (31) Barone, V.; Hod, O.; Peralta, J. E.; Scuseria, G. E. Accurate Prediction of the Electronic Properties of Low-Dimensional Graphene Derivatives Using a Screened Hybrid Density Functional. *Acc. Chem. Res.* **2011**, *44*, 269–279.
- (32) Fuchs, F.; Furthmüller, J.; Bechstedt, F.; Shishkin, M.; Kresse, G. Quasiparticle Band Structure Based on a Generalized Kohn-Sham Scheme. *Phys. Rev. B* **2007**, *76*, 115109.
- (33) Kresse, G.; Joubert, D. From Ultrasoft Pseudopotentials to the Projector Augmented-Wave Method. *Phys. Rev. B* **1999**, *59*, 1758–1775.
- (34) Blochl, P. E. Projector Augmented-Wave Method. *Phys. Rev. B* **1994**, *50*, 17953–17979.
- (35) Shishkin, M.; Kresse, G. Implementation and Performance of the Frequency-Dependent GW Method within the PAW Framework. *Phys. Rev. B* **2006**, *74*.
- (36) Gajdos, M.; Hummer, K.; Kresse, G.; Furthmüller, J.; Bechstedt, F. Linear Optical Properties in the Projector-Augmented Wave Methodology. *Phys. Rev. B* **2006**, *73*, No. 045112.
- (37) Rohlfing, M.; Louie, S. G. Excitonic Effects and the Optical Absorption Spectrum of Hydrogenated Si Clusters. *Phys. Rev. Lett.* **1998**, *80*, 3320–3323.
- (38) Rohlfing, M.; Louie, S. G. Electron-Hole Excitations and Optical Spectra from First Principles. *Phys. Rev. B* **2000**, *62*, 4927–4944.
- (39) Fuchs, F.; Rodl, C.; Schleife, A.; Bechstedt, F. Efficient  $O(N^2)$  Approach to Solve the Bethe–Salpeter Equation for Excitonic Bound States. *Phys. Rev. B* **2008**, *78*, No. 085103.
- (40) Rüdorff, W., Graphite Intercalation Compounds. In *Advances in Inorganic Chemistry and Radiochemistry*; Emcleus, J., Sharpe, A. G., Eds.; Academic Press: New York, 1959; Vol. 1.
- (41) Medeiros, P. V. C.; Mascarenhas, A. J. S.; Mota, F. D.; de Castilho, C. M. C. A DFT Study of Halogen Atoms Adsorbed on Graphene Layers. *Nanotechnology* **2010**, *21*, 485701.
- (42) Yang, M. M.; Zhou, L.; Wang, J. Y.; Liu, Z. F.; Liu, Z. R. Evolutionary Chlorination of Graphene: From Charge-Transfer Complex to Covalent Bonding and Nonbonding. *J. Phys. Chem. C* **2012**, *116*, 844–850.
- (43) Wu, J.; Xie, L. M.; Li, Y. G.; Wang, H. L.; Ouyang, Y. J.; Guo, J.; Dai, H. J. Controlled Chlorine Plasma Reaction for Noninvasive Graphene Doping. *J. Am. Chem. Soc.* **2011**, *133*, 19668–19671.
- (44) Ijas, M.; Havu, P.; Harju, A. Fracturing Graphene by Chlorination: A Theoretical Viewpoint. *Phys. Rev. B* **2012**, *85*, 035440.
- (45) Wen, X. D.; Yang, T.; Hoffmann, R.; Ashcroft, N. W.; Martin, R. L.; Rudin, S. P.; Zhu, J. X. Graphane Nanotubes. *ACS Nano* **2012**, *6*, 7142–7150.
- (46) Marsili, M.; Pulci, O. The Fascinating Physics of Carbon Surfaces: First-Principles Study of Hydrogen on C(001), C(111) and Graphene. *J. Phys. D: Appl. Phys.* **2010**, *43*, 374016.
- (47) Sahin, H.; Ciraci, S. Chlorine Adsorption on Graphene: Chlorographene. *J. Phys. Chem. C* **2012**, *116*, 24075–24083.
- (48) Shishkin, M.; Kresse, G. Self-Consistent GW Calculations for Semiconductors and Insulators. *Phys. Rev. B* **2007**, *75*, No. 235102.
- (49) Ataca, C.; Ciraci, S. Functionalization of Single-Layer  $\text{MoS}_2$  Honeycomb Structures. *J. Phys. Chem. C* **2011**, *115*, 13303–13311.
- (50) Wei, W.; Jacob, T. Electronic and Optical Properties of Fluorinated Graphene: A Many-Body Perturbation Theory Study. *Phys. Rev. B* **2013**, *87*, 115431.
- (51) Byun, Y.-M.; Sofo, J.; Crespi, V. In *GW Study of the Effect of Various Defects on the Band Gap of Fluorographene*, Bulletin of the American Physical Society, APS March Meeting 2012, Boston, Massachusetts; APS: Boston, MA, 2012; p A12.00003.
- (52) Samarakoon, D. K.; Wang, X. Q. Chair and Twist-Boat Membranes in Hydrogenated Graphene. *ACS Nano* **2009**, *3*, 4017–4022.
- (53) Bhattacharya, A.; Bhattacharya, S.; Majumder, C.; Das, G. P. Third Conformer of Graphane: A First-Principles Density Functional Theory Study. *Phys. Rev. B* **2011**, *83*, 033404.
- (54) Banhart, F.; Kotakoski, J.; Krashenninnikov, A. V. Structural Defects in Graphene. *ACS Nano* **2011**, *5*, 26–41.